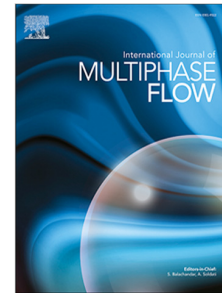# Journal Pre-proof

CFD modeling of droplet permeability in fluidized beds

D.M. Balice, C.W.C. Molenaar, M. Fochesato, C.M. Venier, I. Roghair,
N.G. Deen, M. van Sint Annaland

Please cite this article as: D.M. Balice, C.W.C. Molenaar, M. Fochesato et al., CFD modeling of droplet permeability in fluidized beds. *International Journal of Multiphase Flow* (2022), doi: https://doi.org/10.1016/j.ijmultiphaseflow.2022.104069.

This is a PDF file of an article that has undergone enhancements after acceptance, such as the addition of a cover page and metadata, and formatting for readability, but it is not yet the definitive version of record. This version will undergo additional copyediting, typesetting and review before it is published in its final form, but we are providing this version to give early visibility of the article. Please note that, during the production process, errors may be discovered which could affect the content, and all legal disclaimers that apply to the journal pertain.

CFD modeling of droplet permeability in fluidized beds

D.M. Balice[a,b], C.W.C. Molenaar[a], M. Fochesato[a,f], C.M. Venier[a,d,e], I. Roghair[a,b,*], N.G. Deen[b,c], M. van Sint Annaland[a,b]

[a]*Chemical Process Intensification, Department of Chemical Engineering and Chemistry, Eindhoven University of Technology, P.O. Box 513, 5600 MB Eindhoven, The Netherlands*

[b]*DPI, P.O. Box 902, 5600 AX Eindhoven, the Netherlands*

[c]*Power & Flow Group, Department of Mechanical Engineering, Eindhoven University of Technology, P.O. Box 513, 5600 MB Eindhoven, Netherlands*

[d]*Centro de Investigación en Métodos Computacionales (CIMEC), CONICET, Santa Fe, Argentina*

[e]*Universidad Nacional de Rosario, Facultad de Ciencias Exactas, Ingeniería y Agrimensura, Escuela de Ingeniería Mecánica, Rosario, Argentina*

[f]*Department of Industrial Engineering, University of Padova*

Abstract

The deposition of droplets of size [5 - 22] μm on the surface of particles in a gas-solid fluidized bed has been investigated employing a one-way coupled CFD-DEM modelling. In this approach the gas phase is solved as a continuum and the free-droplets are solved as Lagrangian objects, while solid particles are assumed to be stationary and act as an obstacle for the fluid flow.

In this way, it was possible to calculate the deposition factor, defined as the ratio of droplets deposited on the surface of the particles to the number of droplets injected into the domain as a function of the droplet Stokes number and particle Reynolds number. An empirical correlation was developed that describes the deposition factor as a function of the operating conditions, which is valid for the inertial regime where effects of Brownian motion can be neglected.

The final goal of this investigation is to employ the developed correlation in a larger scale CFD-DEM model describing a polymerization fluidized bed reactor operated in condensed mode, i.e. by injecting liquid into the gas-solid suspension through the gas distributor plate or via nozzles in order to improve the heat management. In this kind of modelling the free-droplets phase is described as a continuum and the deposition rate of droplets determines the amount of liquid on the particle surface, which affects for the hydrodynamic (i.e. formation of liquid bridges between particles) and thermal behavior (i.e. liquid evaporation, kinetic and subsequent cooling effect) of the system.

Keywords: Granular matter, Droplets, Particles, Multiphase Flow, CFD-DEM, OpenFOAM, Fluidized Bed

*Corresponding author: i.roghair@tue.nl

1. Introduction

A fluidized bed with liquid injection is a common choice for various physical and chemical solid operations. Fluidized beds are preferred over other (mechanical) unit operations due to their enhanced heat and mass transfer and intense gas-solid mixing [33, 36]. Examples of processes that use fluidized beds with liquid injection include particle granulation, fluid catalytic cracking (FCC), and polyolefin production. In the first example a liquid binder is atomized and injected into the bed of fluidized particles. The binder sticks to the particle surface forming wet patches and simultaneously evaporates, resulting in a layer-wise progressive particle growth to form bigger granules [48].

In FCC, the reaction takes place in the riser reactor between long-chain hydrocarbons ('oil gas') and hot catalytic particles coming from a regeneration unit. Oil gas is fed as a liquid spray in the bottom of the riser and vaporizes upon contact with hot particles. The generated gas is the main driving force for the solid uprise [27, 42].

In gas-phase polymerization of olefins, active polymer particles are fluidized under reactive operating conditions using a diluted monomer gas. As the reaction takes place, an excessive amount of heat is generated, so large that without an additional cooling mechanism it would limit the production rate [32]. Injecting an inert cooling liquid, often called an induced condensing agent (ICA), provides an effective way of controlling the temperature due to the large latent heat that is associated with evaporation. However, during these processes, a small change in the operating conditions can lead to an imbalance between the rates of liquid deposition and evaporation. This can lead to the formation of agglomerates and local de-fluidization, both contributing to poor bed performance and product quality. Until now, operating conditions and the equipment geometry have mostly been developed empirically and the actual influence of the fundamental mechanisms in the process is not well understood [30, 46]. Detailed knowledge of the mechanism of liquid injection into fluidized bed reactors would be advantageous, not only for an engineering design but also for the safe and economic operation on an industrial scale.

The process of liquid injection in fluidized beds is complex because various phenomena can take place simultaneously and/or in rapid succession. Examples are deposition of droplets on the particle surface, evaporation of liquid from the particle surface, droplets coalescence and breakage, agglomeration due to wet collisions, and liquid binding. To design fluidized beds with liquid injection it is common practice to employ greatly simplified models. For example, in the case of granulation, the entire process is often described as a combination of only three sets of processes: wetting and nucleation, consolidation and growth, and attrition and breakage [19].

Those processes are then modeled resorting to population balances, in which various empirical models of coalescence and breakage are used to predict the extent of granulation [17]. The main flaw of this approach is that it heavily depends on empirically fitted parameters. In attempts to more accurately describe the granulation process, more sophisticated models have been developed. However, as such models become more advanced, the connection with underlying physics driving the process becomes more tenuous. Iveson [18] suggests that this could be an area of application for which population balances methodology is not suited and that the use of CFD combined with discrete element modeling (DEM) may be more appropriate.

2

In CFD-DEM of fluidized beds, the gas-phase is treated as a continuum (Eulerian) phase and described by Navier-Stokes equations, whereas the particulate phase is modeled as individual discrete entities (Lagrangian phase) and governed by Newton's second law. As each particle is tracked individually, the method allows for a complete representation of the gas-particle, particle-particle, and particle-wall interactions [6]. Several authors have also made attempts at extending CFD-DEMs to model the process of liquid injection in fluidized beds.

Goldschmidt et al. [14] were one of the first in their attempt to model liquid injection in fluidized beds. In their approach, the injected liquid droplets as well as the particles were treated as discrete elements. To model the agglomeration process, they defined collision laws where collisions between droplets and particles would result in the formation of wet particles. Encounters between dry particles were handled using a traditional hard-sphere contact model and interactions between a dry particle and a wet spot on a wet particle would always result in agglomeration of the two entities. In practice, however, this assumption is not always valid. Also, the model was limited to a 2D Cartesian geometry and the number of discrete elements solvable with a realistic computational time was much lower than necessary for systems of experimental relevance.

Sutkar et al. [50] developed a CFD-DEM model for coupled heat and mass transfer in spout fluidized beds with liquid injection. In their work, simulations were performed using glass particles, showing a fair agreement with experiments in terms of particulate flow pattern, pressure drop, and particle velocities. However, these simulations were performed under the assumption that droplets form a uniform liquid layer around the particles (neglecting partial wetting), that no droplet breakage occurs and are limited to a relative small liquid injection rate ($O(10^6)$ droplets/s).

More recently Jiang et al. [20] developed a CFD-DEM model for a Wuster fluidized bed coater by injecting solid-like droplets in a predefined spray zone to investigate the particles and droplets residence time and collision velocity in a . Similarly Jiang et al. [21] developed a CFD-DEM-Monte Carlo model for the same system. In both cases authors found good agreement with available experimental data, but employed a relatively small droplets flowrate ($O(10^5) - (10^6)$ droplets/s).

Nevertheless, the above authors demonstrate that with the use of realistic contact models and particle bonding interactions, a CFD-DEM model is in principle capable of simulating both the consolidation and growth as well as the attrition and breakage processes. The main drawback of this approach is the description of droplets as discrete elements. To model a spray, the calculation of every single droplet trajectory is required, making this approach practically inapplicable to a large system and capable only to replicate laboratory-scale experimental equipment.

Some authors have attempted to exclude droplets as a discrete entity and model wetting and nucleation in a different way. An example of such an approach is demonstrated by Kafui and Thornton [22], presenting a 3D model of a fluidized-bed spray granulator without the presence of discrete droplets. In their work, the presence of liquid on a particle is modeled in terms of surface energy, where particles that are wetted gain surface energy according to their position and residence time inside a predefined spray zone. This surface energy is then used to calculate a time-dependent adhesion force between wet particles. Although the authors use conceptional notions of wetting and drying, they also emphasize that these are not equivalent to model an actual liquid

3

binder. In addition, this approach requires an estimated guess of a spray zone, which limits the possibility of taking account of the local, time-dependent flow conditions (e.g. presence of bubbles, turbulence, etc.). Given the shortcomings of presented approaches in current literature, it is anticipated that improved methods that allow to obtain accurate results when they capture the underlying phenomena without a significant increase in computational effort.

To overcome the limiting factor of existing modeling techniques, a novel approach based on the idea of multi-scale modeling is presented. In the concept of multi-scale modeling, closure equations are derived from detailed small-scale simulations and used in large(r)-scale simulations. By doing this, it is possible to accurately capture small-scale phenomena on a larger scale without resolving these. Specifically, the envisioned scale-up of liquid injection modeling in fluidized beds can be achieved by treatment of the droplets as a continuum (e.g. droplet phase fraction as part of the continuous gas phase), albeit with the distinction between separate phases such as vapor, free, and deposited droplets.

Treating droplets as a continuum is much faster than describing each small droplet as a discrete entity, and has the additional benefit that it also allows for coarse-grained (phenomenological) coupling to the mass and energy balances that can be taken into account in CFD-DEM simulations, for instance accounting for effects of evaporation and condensation. However, an aspect still missing for this technique is how freely moving droplets interact with the solids phase, specifically the fraction of droplets that hit the particles surface when moving with the interstitial gas flow, as opposed to droplets that remain dispersed in the gas phase. Indeed, this aspect dictates the evolution of the liquid layer volume (or liquid patch size) present on particle surfaces, and therefore the solid-liquid heat transfer due to conduction and evaporation.

The deposition of droplets and small particles in fluidized and fixed beds has been object of literature studies in the context of granular filtration both from an experimental and modelling perspective. For example both [39] and [8] developed a mathematical model to simulate particulate removal in a gas-solid fluidized bed by combining a three-phase (bubble, cloud and emulsion) approach for the description of the gas-solid hydrodynamics combined with a droplet deposition model developed for a single particle. It is important to note that in this work it was assumed that every particle is stationary, surrounded by a gas flow in Stokes' regime and acts as an independent collector with a collection efficiency depending on what is the main deposition mechanism for each droplet size (viz. Interception, Impaction, Brownian motion and Induced Electrostatic Forces). A similar model for the calculation of fine droplet deposition rate in fluidized beds was developed in [54], with the main difference that the capture efficiency is calculated based on the local relative phase velocities and by employing the constricted tube model [38] for the description of the gas in the emulsion phase. In [53] a mathematical model for the capture of fine dust in fluidized bed was developed, calculating the diffusional capture factor for a single spherical particle (with the assumption of steady-state Stokian gas motion) and correlating it to the overall capture efficiency of the fluidized bed. While all the presented models show a fair agreement among them and with experimental data, they are not capable of describing the motion of the gas, and as a consequence of droplets, in the voidage of a fluidized bed, where particles are often in contact and the assumption of uniform gas flow in Stokes regime is strictly no longer valid.

Several experimental works have been published on the collection of aerosols in fluidized

4

beds [24, 31, 45], but these all focus on micronic and sub-micronic droplets (with the exception of one set of data reported in [24]), since this is the size of interest in the context of filtration.

In this work we study the fate of relatively large inertial droplets (5-22 μm) moving through a complex space made up from the interstitial volume between much larger particles. Note that we did not consider very small droplets where Brownian diffusion is important, because in the systems at hand such droplets would very quickly evaporate. Consequently the presented results should not be applied for the case of Browian droplets ($< 0.1 \mu m$).

To obtain better insight in how droplets move through the interstitial space, which droplet paths terminate on a particle surface and which ones move on, direct numerical simulations (DNS) are suited. In DNS, all relevant time and length scales are resolved without making any assumptions, meaning that no closure equations are required: in this way there isn't an *a priori* imposition of the gas flow characteristics (e.g. assuming a laminar flow). Starting from these first principles, it allows us to study the penetration of liquid droplets through fluidized arrays of particles, and to describe the general behavior in the form of a closure correlation.

In this study, the droplet permeability of a fluidized bed was investigated with the aim of developing a correlation for the rate of deposition of liquid droplets on the particle surface. This was done by importing a 'frozen' particle spatial configuration from a CFD-DEM simulation into OpenFOAM. Then, the domain was meshed and the gas flow was calculated. Finally, tracer droplets were injected into the domain and their trajectory was calculated. This allows for the calculation of the deposition factor(σ) as the ratio between the number of droplets deposited on the surface of the particles and the number of droplets injected into the domain. This procedure has been reiterated for several systems differing in droplet size, particle position, and flow conditions. In this work, the detailed modeling methodology is presented, together with several verification cases to demonstrate the validity, accuracy, and reproducibility of the model. Subsequently, a method for a generalized use of this technique is presented. Finally, obtained results are presented in the form of a correlation which can be used to describe the deposition of discrete droplets using a continuum approach, and compared with experimental data from literature.

2. Methodology

In this work, the deposition of droplets on the particle surface was investigated developing a novel liquid injection model. The model is an Euler-Lagrange type of CFD model and was developed within the open source CFD framework OpenFOAM v7 [12]. The geometry of the computational domain is built as a static array of solid particles, acting as obstacles for the gas and droplets motion. At the start of the simulation the gas motion is calculated, then liquid droplets are injected into the domain from random locations distributed at the bottom face with a velocity equal to the local velocity of the gas phase. Because of their high relaxation time the solid particles are considered stationary and treated as static walls. The physical properties of the system were chosen in order to mimic a fluidized bed ethylene polymerization process (FBR in condensed mode operation). A list of the relevant physical parameters is presented in Table 1.
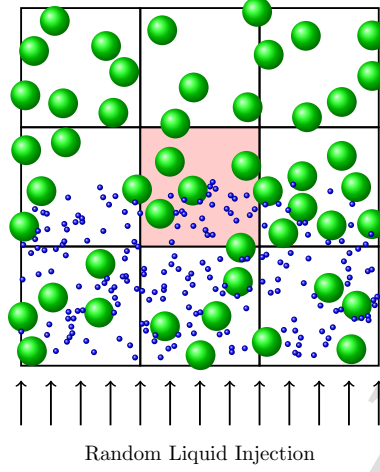
5

Figure 1: Visualization of the approach for liquid injection simulations using domain generated with a discrete particle model, where the deposition of droplets is investigated in the central reference cell (red)

Table 1: Physical parameters used in the simulations

Property	Value	Unit
ρ_f	15.43	$\mathrm{kg\,m^{-3}}$
ρ_d	655	$\mathrm{kg\,m^{-3}}$
μ_f	$1.44 \cdot 10^{-5}$	$\mathrm{kg\,m^{-1}\,s^{-1}}$
d_p	$5 \cdot 10^{-4}$	m
Re_p	[100 - 350]	-
ε	[0.4 - 0.8]	-
Stk	[0.02 - 12]	-
Re_{pore}	[35 - 2000]	-

The range for the particle Reynolds number ($Re_p = {}^{d_p v_0 \rho_f}/_{\mu_f}$, with v_0 being the gas superficial velocity) and porosity is based on the work of Li et al. [28], where the effect of the superficial gas velocity on the bed hydrodynamics was investigated. From these simulations, it was concluded that at a velocity corresponding to the minimum fluidization velocity ($u_{mf} \approx 0.3$ m s^{-1}), the first small spherical bubbles start to form, while for superficial velocities > 2.5 u_{mf}, the typical bubble structure is lost. Moreover, Li et al. [28] also found that a typical range for porosity $\varepsilon = 1 - \phi$ encountered in an FBR is $0.4 \leq \varepsilon \leq 0.8$. Consequently, based on these findings, those two ranges were also adopted for simulations presented in this work. The range for the droplet Stokes number ($Stk = {}^{\rho_d d_d^2 v_i}/_{18 \mu_f d_p}$, with v_i being the average interstitial gas velocity) is chosen to represent a possible droplet size distribution.

6

2.1. Domain generation

The first step in simulating the deposition of droplets on the particle surface is the generation of a suitable simulation domain. Typical particle configurations in fluidized beds are generated with the help of an extensively used and validated in-house CFD-DEM [5, 34, 51].

The deposition rate is investigated in a small subdomain with dimensions 3.33 mm × 2.9125 mm × 3.0 mm (D x W x H) which is divided in multiple grid cells: 1) A central cell, typically on the order of 2-3 times the particle diameter, in which the deposition of droplets is investigated, and 2) 26 cells, surrounding the central cell in all directions (including corners). Preliminary simulations have shown that the surrounding cells are necessary to catch pre-channeling of the droplets: while droplets are injected uniformly through the bottom face, the presence of particles channels their movement via preferential pathways. Injecting droplets directly in the central cell would result in loss of model accuracy. Moreover, using surrounding cells allows to take into account droplets traveling through the lateral faces of the central cell and reducing the influence of boundary conditions on the gas flow calculated in the central cell.

For the purpose of this work, the investigated domains are characterized with a single value of porosity: while in a fluidized bed a range of porosities can be found, it is common practice to define it locally as a single value. This approximation is valid for the typical size of computational cells considered in this work, but may lose validity for much larger domains. The presence of low and high porosity zones in the reactor (e.g. bubbles) can be accounted for in larger scale CFD-DEM models that use the results of this work as a closure correlation.

2.2. Mesh generation

The CFD-DEM subdomain is then imported into OpenFOAM, where the domain is meshed using the built-in mesh generation utility snappyHexMesh [13]. This utility initially builds a purely hexahedral base mesh, which is then refined using the octree approach where each cell in close vicinity of the solid particles is divided one or more times, refining the mesh to the desired level. In the first stage of the meshing process, a castellated mesh approximates the shape of the particles in a stair-step way. The next step involves moving cell vertex points onto the nearest surface boundary with the help of a so-called snapping algorithm. The final mesh generated by adopting this strategy is predominantly hexahedral with only a small percentage of polyhedral elements near the boundary walls. The use of snappyHexMesh is common in scientific literature and previous studies indicate that this is an effective and accurate tool for meshing complex geometries [7, 16, 29].

2.3. Resolution requirements

In DNS, the Navier-Stokes equations are numerically solved without employing any turbulence model, this means that the whole range of relevant spatial and temporal scales of turbulence must be resolved. While this approach avoids an imposition of the gas flow characteristics, it poses a very stringent requirement on the grid size because the size of the mesh elements should be small enough to resolve the smallest dissipative motion, and consequently limits the maximum simulation domain size.

7

To fully resolve the smallest scale, the mesh size h should be smaller than the Kolmogorov length scale ($h < \eta$) [40]. Research has shown however, that this requirement is probably too strict as most of the dissipation takes place at scales that are substantially larger than the Kolmogorov scale, say 5η–15η [35].

An a priori estimation of the Kolmogorov scale is however only limited to simple cases as it is difficult to obtain detailed time and space resolved velocity data in complex geometries. In this work, the estimation of the Kolmogorov scales is based on the work of Patil and Liburdy [37]. In this study, the authors performed time-resolved Particle Image Velocimetry measurements of turbulent flow in porous media, determined characteristic velocity, length, and time scales and related them to the pore Reynolds number (Re_{pore}). They found that if Re_{pore} is sufficiently high ($Re_{\text{pore}} \approx 1000$) the scales reach an asymptotic value which can then be estimated by:

$$\frac{\eta}{D_h} = 1.32\, Re_{\text{pore}}^{-3/4} \tag{1}$$

where the pore Reynolds number is defined as:

$$Re_{\text{pore}} = \frac{D_h\, U}{\nu_f} \tag{2}$$

with D_h the hydraulic diameter; $D_h = \frac{2}{3}\frac{\varepsilon}{(1-\varepsilon)}\, d_p$.

Given the range of parameters in the presented simulations, the gas flow will be mostly represented in the transitional regime from laminar to turbulent flow [3, 56]. In such regime, this correlation is strictly speaking no longer valid. However, for lower Reynolds numbers, the energy dissipation rate becomes lower, resulting in a larger Kolmogorov scale. The correlation presented in Eq. 1 therefore provides a lower limit for the required grid resolution.

Moreover, instead of adopting multiple mesh resolutions for the different simulations, a single mesh resolution based on the most stringent operating conditions (smallest scale), was used for all simulations. The size of the base mesh elements was chosen to be on the order of 7-8 η. The number of refinements and so the final mesh density was then determined by conducting a grid dependency analysis, to properly resolve the relevant scales and to guarantee the independence of the CFD solution from the grid size.

2.4. Modeling of continuous phase

The governing equations of the gas are the continuity (Eq. 3) and momentum equations (Eq. 4) for Newtonian and incompressible flows [11]:

$$\nabla \cdot \mathbf{u} = 0 \tag{3}$$

$$\frac{\partial(\rho_f \mathbf{u})}{\partial t} + \nabla \cdot \rho_f(\mathbf{u}\mathbf{u}) = -\nabla \cdot \boldsymbol{\tau} - \nabla p + \rho_f \mathbf{g} \tag{4}$$

The initial condition for the gas flow field was set to be equal to the inlet velocity, whereas the pressure field was initialized with a zero relative pressure. The boundary conditions for the gas-phase are listed in Table 2.

8

Table 2: Boundary conditions for the gas-phase

	u	p
inlet	fixed value	zero gradient
outlet	zero gradient	fixed value
lateral sides	free slip	free slip
particles	no slip	zero gradient

For the temporal discretization, a second-order implicit Crank-Nicolson scheme was adopted. Similarly to the grid resolution requirements, the time step must also be sufficiently small to resolve the smallest time scales. The temporal resolution however was not estimated based on the Kolmogorov time scale, but instead was set to ensure that the maximum Courant number did not exceed the value of 0.9. In OpenFOAM, the spatial terms are discretized using a finite volume method. For the discretization of the convective term a limited third order interpolation scheme was used (limitedCubicV), i.e. a bounded higher-order scheme that takes into account the flow field direction [12].

2.5. Liquid injection model

The purpose of this work is to study the permeability of a fluidized bed in a statistical manner by injecting multiple droplets at once, characterizing the rate of deposition. At the start of a liquid injection simulation, the motion of the gas is first calculated. Subsequently, Lagrangian tracer droplets are injected from a randomly distributed location at the inlet with a velocity equal to the local velocity of the gas phase, and the droplets fate is examined. In this section, the governing equations for the Lagrangian phase as well as the coupling and solution strategy for the liquid injection simulations are outlined.

2.5.1. Modeling of Lagrangian phase

The motion of dispersed liquid droplets are governed by Newton's second law of motion (Eq.5)

$$m_d \frac{d\mathbf{v}_d}{dt} = \mathbf{F}_{tot} \tag{5}$$

where the total force acting on a droplet is the sum of gravity, buoyancy, drag and pressure forces (no Brownian motion has been taken into account, which is valid for droplets with $d_d \gg 1\mu m$ [8, 15]).

$$
\begin{aligned}
\mathbf{F}_{tot} = &\left(\rho_d - \rho_f\right) V_d\, \mathbf{g} + \\
&\frac{1}{2}\, \rho_f\, C_D\, A_d\, |\mathbf{u} - \mathbf{v}_d|(\mathbf{u} - \mathbf{v}_d) + m_{f,i} \frac{D\mathbf{U}}{Dt}
\end{aligned}
\tag{6}
$$

Where $\frac{D\mathbf{U}}{Dt} = \frac{\partial}{\partial t} + \mathbf{u} \cdot \nabla$ is the material derivative of the gas evaluated at the particle position and C_D the drag coefficient calculated with the Schiller and Naumann correlation (Eq. 7) [44].

$$C_D = \frac{24}{Re_d} f_{\text{Re}} \tag{7}$$

and

$$f_{\text{Re}} = 1 + 0.15 Re_d^{0.687} \tag{8}$$

9

With the assumption of $\rho_f \ll \rho_d$, Eq. 5 reduces to:

$$\frac{d\mathbf{v}_d}{dt} = \mathbf{g} + \frac{1}{Stk}\frac{f_{Re}}{d_d}(\mathbf{u} - \mathbf{v}_d)^2 \qquad (9)$$

This shows that for small droplets the motion is mostly governed by the droplet Stokes number, while for larger droplets also the droplet Reynolds number may be important ($f_{Re} \gg 1$).

For both the drag force and the pressure gradient force, the local fluid velocity calculated in the Eulerian framework is required for the evaluation of forces in the Lagrangian framework. To accomplish this, the fluid velocity is interpolated from the 8 neighboring points of the Eulerian grid to the position of the droplet using tri-linear interpolation: if the droplets are smaller than the mesh, the presented point-droplet approach is the commonly accepted way of describing droplets motion, whereas for droplets larger than the mesh a droplet-resolved simulation would be more accurate. This would make the simulations particularly computationally expensive, so in such cases it is customary to also use a point-droplet approach at the price of a somewhat lower accuracy. In the presented work droplets are smaller than the mesh size in almost every presented case, with some exceptions for the cases with larger droplets where a maximum droplet size to mesh size ratio of $\simeq 2$ is reached. Therefore a point-droplet approach could be employed with a minimum loss of accuracy.

2.5.2. Coupling of liquid droplets

To describe the interaction between the droplets and fluid, a one-way coupling mechanism was selected. This means that the fluid can exert forces on the droplets, but the droplets do not influence the fluid flow. The choice of coupling mechanism depends on the influence of the dispersed phase on the fluid phase, which is commonly related to the phase fraction. In the case of liquid injection in polyethylene production, the injected droplets rapidly disperse throughout the reactor, resulting in an expected volume phase fraction in the order of 10^{-5} [32]. According to the works of Elghobashi [9] and Balachandar and Eaton [1], with such low phase fractions the dispersed phase has a negligible influence on the fluid flow profiles, nor will there be significant interaction among the droplets, so it is justified to use a one-way coupling scheme. As a result, the flow-field can be solved independently from the Lagrangian droplets, resulting in faster simulations. In addition, because the flow field is unaffected by the presence of the droplets, a large number of droplets can be used to get statistically accurate results.

For more details on the implementation in OpenFOAM, the interested reader is referred to the Appendix.

3. Verification

In this section the results of several verification steps are presented: first a mesh size dependence study, then a verification of the flow solver comparing the resulting drag force exerted on a single particle with its analytical solutions, then a verification of the overall grad force exerted by the fluid on the particle bed with common empirical correlation are preformed. Later an analysis of possible transient characteristic of the gas flow is presented. Finally the influence of particle configuration on the droplets phase behavior

10

is analyzed, followed by a discussion on the possibility of using an artificially-created domain.

3.1. Grid dependence study

To ensure the mesh is sufficiently refined for the flow field calculation a grid dependence study was performed. In this study, a coarse base mesh is created according to the criteria mentioned in Section 2.4. The mesh was then additionally refined in the close vicinity of the particles until convergence of the local velocity profile was achieved. This was done for a set of three meshes with varying density and refinements. Then, the local velocity was sampled across a line at the center of the domain ($y = 1.425$ mm and $z = 1.5$ mm), from $x = 0$ to $x = 3.3$ mm. To compare the local velocity between the different grids, the results from the coarse and fine grids were interpolated to the finest grid and are presented in Fig. 2.
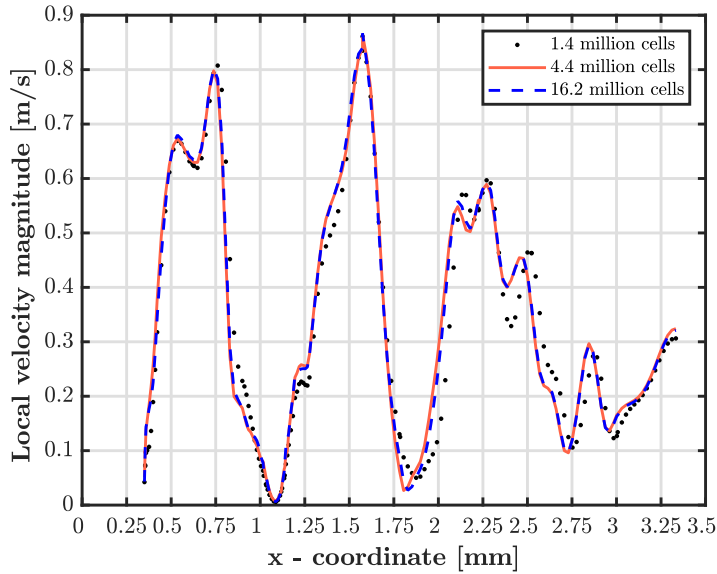

Figure 2: Local velocity sampled across a line at the center of the domain ($y = 1.425\,mm$ and $z = 1.5\,mm$), from $x = 0$ to $x = 3.3\,mm$ for $\varepsilon = 0.65$ and $Re_p = 350$

The mean deviation in local velocity between the coarse grid (1.4 million cells) and the finest grid (16.2 million cells) was found to be approximately 20%, while for the finer (4.4 million cells) and finest grid the difference was $< 4\%$. The finer mesh was found to be a good compromise between accuracy and computational effort and was therefore chosen as a suitable refinement level for the other simulations.

3.2. Flow through an array of spheres

To verify the Eulerian solver, the flow through a periodic simple cubic array of spheres was considered. This problem is interesting for verification, as both Sangani and Acrivos

11

[43] and Zick and Homsy [55] have derived analytical solutions to the Navier-Stokes equations in the case of creeping flow ($Re_p < 1$). With these solutions, expressions for the non-dimensional drag force exerted on the array of spheres were derived for the entire range of particle volume fractions $0 \leq \phi \leq \frac{\pi}{6}$. In literature, two definitions of drag force arise [2]: the drag force can be defined as the total force arising from gas-solid interaction ($\mathbf{f_{g \rightarrow s}}$) or as the local frictional force ($\mathbf{f_d}$). The two definitions differ by a factor $(1 - \phi)$. The relation between the pressure drop and the drag force can be derived from a force balance and is presented in Eq. 10.

$$\mathbf{f}_{g \rightarrow s} = \frac{\mathbf{f}_d}{1 - \phi} = -\frac{V_p \nabla P}{\phi} \tag{10}$$

It is common to present the force in non-dimensionless form by normalizing it with the Stokes drag:

$$F = \frac{|\mathbf{f_d}|}{|\mathbf{f_{Stk}}|} = \frac{|\mathbf{f_d}|}{3 \pi \mu_f d_p (1 - \phi) v_0} \tag{11}$$

Combining Eqs. 10 and 11, F can be written as:

$$F = \frac{\Delta P}{L} \frac{d_p^2}{18 \mu_f \, \phi \, v_0} \tag{12}$$

With $\Delta P / L$ being the pressure gradient over the domain, ϕ the particle volume fraction and v_0 the volume averaged superficial velocity.

In this verification study, the drag expression taken from the work of Sangani and Acrivos [43] is used as comparison. This was done by performing simulations using a simple cubic domain where periodic boundary conditions were applied in all three directions. To set the fluid in motion on a fully periodic domain, OpenFOAM will automatically impose a pressure gradient based on a pre-defined volume averaged mean interstitial velocity. When the simulation starts the solver will then try to iteratively match this mean velocity by changing the pressure gradient accordingly. In those simulations a constant mean interstitial velocity of $1.866 \cdot 10^{-4} \, \mathrm{m\,s^{-1}}$ was selected for all cases, corresponding to a particle Reynolds number of 0.1. After the pressure gradient converged to a constant value, the simulation was stopped, and repeated for different values of porosity up to the maximum possible (SCC)-packing fraction of $\phi_{max} = \frac{\pi}{6}$. This entire process was then repeated with a more refined mesh. The pressure gradient and the mean velocity were then used to compute the non-dimensional drag force according to Eq. 12 which were compared to the results by Sangani and Acrivos [43] and are shown in Fig. 3.
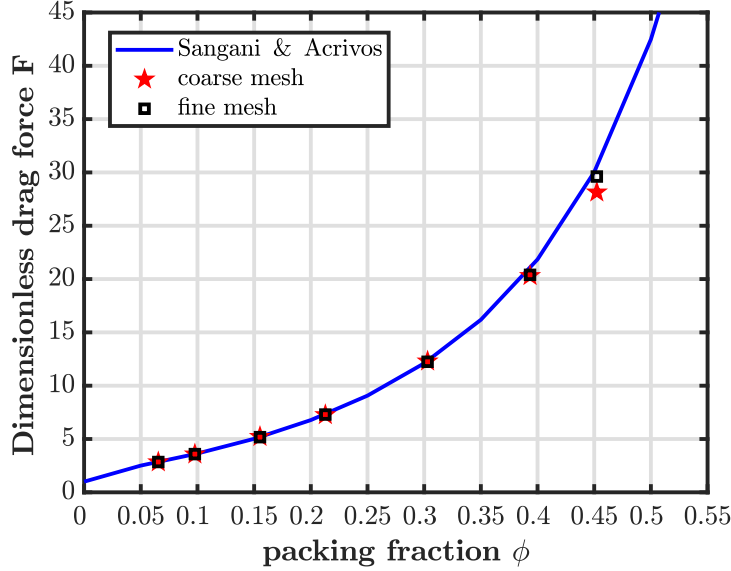
12

Figure 3: Comparison between the dimensionless drag force computed from simulations and the analytical solution for a cubic domain of spheres by Sangani and Acrivos [43] at $Re_p = 0.1$

What can be observed from the figure is that for both coarse and fine meshes, the computed dimensionless drag force closely corresponds to the results by Sangani and Acrivos [43] for the entire porosity range. The mean relative deviation was found to be 1.10 and 0.9 % for the coarse and fine mesh, respectively.

3.3. Drag force comparison

For this second case a similar procedure was adopted, but instead of using analytical expressions, established empirical correlations were used to calculate the non-dimensional drag force. Three different particle configurations from CFD-DEM were considered with porosities $\varepsilon = 0.47$, 0.64 and 0.74. In each of these cases, the mean interstitial gas velocity was varied between 0.3 and $0.7 \, \mathrm{m \, s^{-1}}$ to ensure a proper verification over the entire range of interest. For each porosity value, the drag force computed in the simulations were compared with the empirical correlations using the mean relative deviation (Eq. 13). A summary of the comparison is presented in Table 3.

$$MRD = \frac{1}{N_{sim}} \sum \frac{|F_d^{sim} - F_d^{corr}|}{F_d^{sim}} \cdot 100\% \tag{13}$$

The results show that there are large discrepancies between the simulation results and the drag force predicted by Ergun's equation. The resulting mean relative deviation is 6.7% for a low porosity of $\varepsilon = 0.47$, where the error increases for a higher porosity, reaching 16.8% and 25.3% for a porosity of $\varepsilon = 0.64$ and $\varepsilon = 0.74$, respectively. The large deviations with Ergun equation might be attributed to its range of applicability:

13

Table 3: Comparison of drag correlations with their range of validity and Mean Relative Deviation (MRD) to this work for several porosities.

Correlation	Validity	MRD (%)			Reference
		$\varepsilon = 0.74$	$\varepsilon = 0.64$	$\varepsilon = 0.47$	
Ergun	$\varepsilon < 0.8$	25.3	16.9	7.2	[10]
Beetstra & v.d. Hoef	$Re_p < 1000$	6.7	6.9	4.0	[2]
Tang et al.	$Re_p < 1000$	2.5	2.4	4.1	[52]

while Ergun's equation is usually considered applicable to systems with a porosity up to 0.8, in the experiments used to derive such correlation only a porosity in the range of $0.43 \leq \varepsilon \leq 0.55$ was considered. This could explain why the deviation rises with increasing porosity. When the results are compared to correlations with a larger range of applicability such as the one derived by Beetstra et al. [2] and Tang et al. [52], it can be found that the maximum mean relative deviation is only 6.9 % and 4.1 % for Beetstra's and Tang's correlation respectively. This is comparable to what was found in their studies, from which it can be concluded that the flow field is adequately resolved to produce accurate results.

3.4. Analysis of transient flow behavior

In most of the preliminary simulations it was found that the gas motion converges to a laminar flow. In some occasions however, transient characteristics of the flow were observed. An example of such a case is depicted in Fig. 4. In this simulation, "sample-probes" were randomly placed throughout the domain to investigate the flow field at a particle Reynolds number of 350 and a porosity of $\varepsilon = 0.7$. The simulation end time was set to $t = 0.04$ s which is approximately equal to 10 times the residence time τ. As seen in Fig. 4, the flow clearly shows transient behavior. Moreover, for a time $t < 0.005$ s (≈ 2 τ) the flow shows an irregular transient behavior, while for a time $t > 0.005$ s it seems to reach a statistically steady-state, where the fluctuations follow a pseudo-periodic pattern.
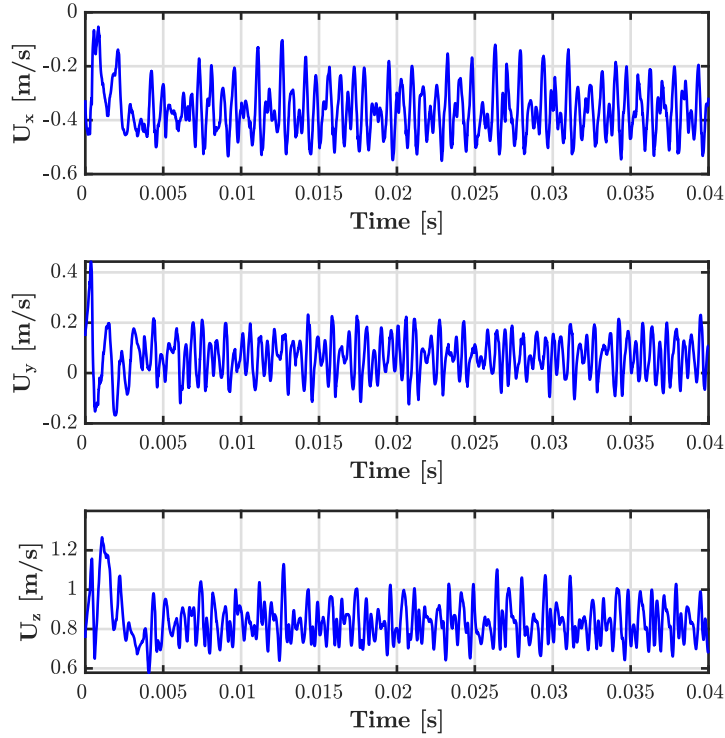
14

Figure 4: Transient evolution of the gas-velocity components (x, y, z) at a particular probe location for $Re_p = 350$.

To investigate the effect of the transient flow behavior on the droplets deposition, a series of simulations where droplets were injected at different times were performed. Then, an additional droplet injection simulation was performed using the time-averaged flow field of the gas. This test has been repeated twice, one for small droplets with a diameter of $d_d = 5$ µm and one for larger droplets with $d_d = 22$ µm. It is expected that the finer droplets, having a smaller Stokes number, should be more affected by the transient characteristics of the flow. The results of both cases, along with the time-averaged results are reported in Table 4.

Table 4: Time dependence of droplet deposition for droplet sizes $d_d = 5$ µm and $d_d = 22$ µm

15

Time of Injection [s]	deposition factor	
-	$d_d = 5$ µm	$d_d = 22$ µm
0.006	0.3063	0.806
0.011	0.3054	0.8058
0.016	0.30625	0.8046
0.021	0.3056	0.8043
time averaged	0.3103	0.8061

It was observed that for both large and small droplets there is no noticeable difference in the deposition factor for different injection times in the periodic transient phase. A small but acceptable difference arises in comparison with time-average simulations.

3.5. Number of droplets injected

The purpose of this work is to investigate the statistical behavior of droplets. Therefore, it is of paramount importance that the number of injected droplets is large enough to provide statistically sound results. For this reason, the influence of the number of droplets injected into the domain was analyzed by performing preliminary simulations. The analysis is carried out by systematically increasing the number of droplets injected into a domain with a porosity equal to $\varepsilon = 0.65$. The inlet velocity was set to $0.6 \, \mathrm{m\,s^{-1}}$ and droplets of 22 µm were injected. Each simulation was repeated three times. The results are presented in Fig. 5, where the dots represent the average results and the error bars represent the standard deviation among the three simulations.
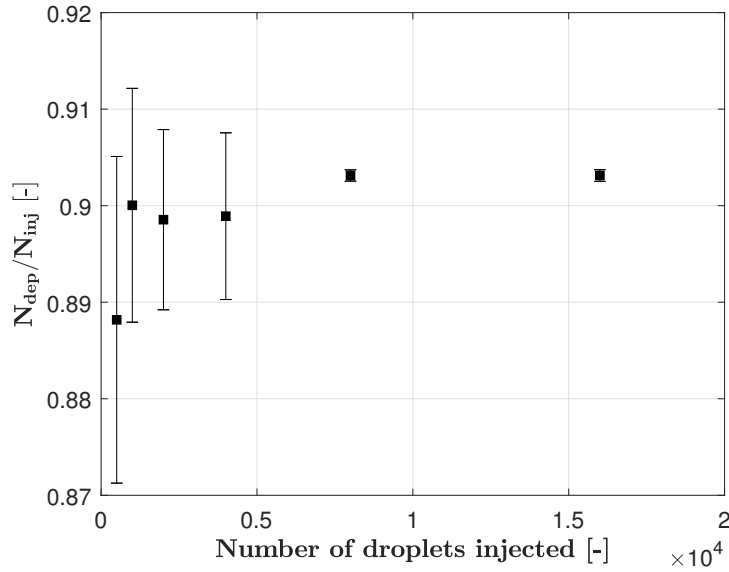

Figure 5: The effect of number of injected droplets on the measured deposition factor $N_{\mathrm{dep}}/N_{\mathrm{inj}}$

16

In this figure, it can be seen that, as the number of droplets is increased the deposition factor, the ratio of droplet paths that terminate at a particle surface vs. the total number of injected droplets $N_{\mathrm{dep}}/N_{\mathrm{inj}}$, tends to an asymptotic value. Looking at the standard deviation, it can be seen that this also reduces the statistical error, which is in agreement with the principles of a Monte-Carlo approach. Consequently, the number of injected droplets should be as high as possible. However, as the number of droplets is increased, this also leads to higher computational expenses. This results in a trade-off between reducing statistical error and/or increased computational time. As a result of this investigation it was concluded that $8 \cdot 10^3$ is a sufficiently large sample size, with a coefficient of variation lower than 0.1%. Since the calculation of droplets movement is computationally not very expensive, $2 \cdot 10^4$ droplets were used in this work in order to have a larger statistical population (resulting in a coefficient of variation of $< 0.07\%$).

3.6. Dependence on particle configuration

The particle configuration generated by the CFD-DEM serves as a basis of various sub-domains with similar porosity but different particle arrangement. To test the consistency of the model and highlight an eventual dependence of the deposition factor on the particle configuration, simulations were performed using a constant porosity while selecting different particle configurations. In total, 5 of such simulations were performed using a fixed gas inlet velocity of $0.6 \mathrm{~m\,s^{-1}}$, a droplet diameter of 22 µm and a porosity of $\varepsilon = 0.65$. The obtained deposition factor is summarized in Table 5.

Table 5: Data for consistency test at a porosity of $\varepsilon = 0.65$

Simulation Nr.	Deposition factor σ
1	0.924
2	0.8993
3	0.8319
4	0.8577
5	0.9229
Mean	0.8872
Std.dev.	0.04094

As seen from the table, all the particle configurations lead to a similar deposition factor, with an average value of 0.8872 and a standard deviation of 0.041: this indicates that the deposition of droplets is only weakly dependent on the geometric particle arrangement. To further investigate the influence of the particle configuration, the same series of simulations were repeated for two more sets of CFD-DEM generated domains with porosities of $\varepsilon = 0.8$ and $\varepsilon = 0.5$, confirming the small dependence of the deposition factor on the particle configurations. The results are summarized in Fig. 6.
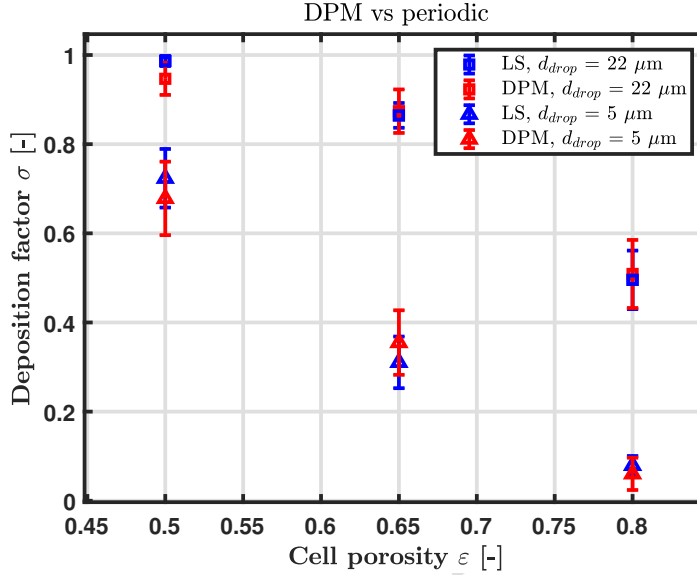
17

Figure 6: A comparison between the deposition factor for different particle configurations generated by the CFD-DEM and artificially created by the Lubachevsky-Stillinger (LS) algorithm, for two droplet diameters $d_d = 22$ µm and $d_d = 5$ µm and three cases with a porosity of $\varepsilon = 0.5$, $\varepsilon = 0.65$ and $\varepsilon = 0.8$

3.7. Periodic domains

The weak dependence of the deposition factor on particle arrangements opens the possibility of using artificially generated geometries with periodic boundaries. With such domains, the additional hassle of generating a fluidized bed CFD-DEM particle arrangement becomes unnecessary. Moreover, if the particle configuration is symmetric with respect to the domain boundaries, periodic boundary conditions can be implemented. By imposing periodicity on the Lagrangian phase, each droplet that leaves through the lateral sides re-enters at the opposite side. As a consequence, the supporting cells that account for lateral droplets in the current approach, become redundant and the domain size can be reduced significantly. In addition, by applying periodic boundary conditions for the gas, possible effects of the free slip boundary conditions at the lateral sides are minimized. For the case of generating a uniform random distributed periodic packing, the Lubachevsky-Stillinger (LS) algorithm was adopted. This allows the generation of a particle packing which is random but symmetric on the external faces. Its implementation was accomplished by modifying the code developed by Skoge et al. [47] to include the generation of non-cubic domains.

For the Lagrangian solver settings, the interaction with lateral sides was changed from "escape" to "none", which allows the droplets to be translated periodically to the opposite face of the domain.

3.8. Generating a periodic domain for liquid injection simulations

When generating a periodic domain, two aspects require special attention: 1) possible droplets pre-channeling has to be allowed; 2) the number of particles in the domain should be large enough to have a random spatial distribution of the particles.

In order to allow droplets pre-channeling it was decided to adopt a structure for the periodic domain similar to the domains generated from the CFD-DEM simulations, i.e. employing two supporting cell surrounding the reference cell in the stream-wise direction, as depicted in Fig. 7. This approach allows for the deposition of droplets to be investigated in a central region of the geometry, taking the channeling effect described in section 2.1 into account.
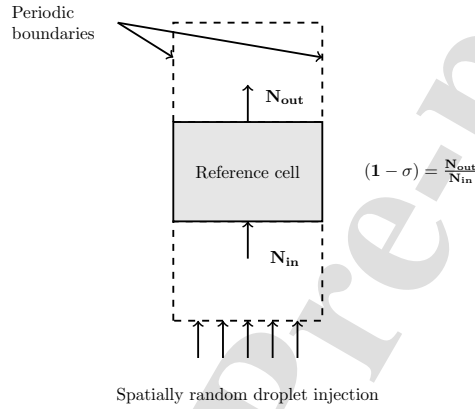

Figure 7: Depiction of simulation domain for periodic boundary condition with a periodic particle arrangement.

In assessing the domain size two contrasting phenomena have to be taken into account: the domain should be large enough to generate a uniform random particle configuration (if the domain is too small the periodicity constraint on the external faces will lead to a non uniform particle spatial distribution), but small enough to keep the simulation time acceptable. A series of simulations were performed where the width and length of the domain were increased systematically from $L/d_p = 2$ to $L/d_p = 4$, while the height was kept at a constant value of $L/d_p = 6$. For each domain size, three different particle arrangements with a constant porosity of $\varepsilon = 0.65$ were generated using the LS-algorithm. At each simulation the inlet gas velocity was set to $0.6\,\mathrm{m\,s^{-1}}$ and droplets of size $d_d = 11.3$ µm were injected.

Table 6: Average deposition factor and standard deviation calculated for different domain size

$L/d_p \rightarrow$	2 x 2 x 6	3 x 3 x 6	4 x 4 x 6
σ_{avg}	0.7474	0.7782	0.766
std. dev.	0.0977	0.0412	0.0461

The results of these simulations (summarized in Table 6) show that, while the average deposition factor is similar for all domain sizes, the smallest domain $2 \times 2 \times 6$ (L/d_p)

19

$(W \times L \times H)$ is affected by large variations resulting in a standard deviation of 0.0977. For the bigger domains the standard deviation is at least a factor 2 smaller and does not change when the domain is enlarged even more. This indicates that the smallest domain is too small to generate an uniform random packing, and thus causing large deviations as a result of preferential pathways. The other domains are sufficiently large to generate a uniform random packing and the remaining standard deviation is probably caused by the differences in particle arrangements. Therefore, the domain size for the rest of the simulations in this study was selected to be $3 \times 3 \times 6$ (L/d_p).

3.9. Periodic vs CFD-DEM particle configurations

The dependency of the deposition factor on the particle configuration was further investigated by performing liquid injection simulations using both periodic and CFD-DEM configurations under identical conditions of porosity, inlet velocity, and droplet size.

Three cases with a porosity of $\varepsilon = 0.5$, $\varepsilon = 0.65$ and $\varepsilon = 0.8$ were considered. For each porosity, five generated particle configurations and five CFD-DEM particle configurations were investigated. All simulations were performed for two droplet sizes of $d_d = 22$ µm and $d_d = 5$ µm with a constant inlet velocity of 0.6 m s^{-1}. The results are summarized in Fig. 6, where the symbols indicate the mean deposition factor for homologous simulations and the error bars show the standard deviation within the series.

As seen in the figure, CFD-DEM and periodic generated configurations lead to very similar results over the entire investigated range. This further substantiates the fact there is only a limited effect of the particle configuration on the deposition factor. It can also be seen that the standard deviation is on average slightly higher for CFD-DEM domains than for periodic domains. This could be attributed to intrinsic heterogeneities of the CFD-DEM particle configurations: while in periodic domains the porosity is uniformly distributed in the whole cell, CFD-DEM configurations can have zones of higher or lower porosity.

4. Results

In this section the simulation results using the liquid injection model are presented. The permeability of the particle configuration is characterized by the deposition factor, which is defined as the ratio between the number of droplets that are deposited on the particle and the number of injected droplets:

$$\sigma = \frac{N_{dep}}{N_{inj}} \tag{14}$$

First, the dependence of the deposition factor on the local porosity, particle Reynolds number and Stokes number are presented and analyzed. Then, the possibility to combine the deposition factor of multiple small-scale simulations to emulate larger scale simulations was investigated. Finally, a nonlinear regression of the obtained simulation data was performed.

4.1. Influence of porosity

The influence of the local porosity was investigated by performing simulations on periodic domains with varying porosity values, a constant gas inlet velocity of $0.6\,\mathrm{m\,s^{-1}}$, and repeated for droplet diameters of 5, 8.2, 22, 33, and 40 µm. From the results, shown in Figure 8, it can be seen that there is a strong influence of the cell porosity on the deposition factor, which is in good agreement with physical expectations: at a lower porosity, the probability of a droplet depositing on a particle surface increases as there are more obstacles to deposit on. Equally, at a higher porosity, the probability for a droplet to encounter a particle decreases, allowing droplets to escape the domain more easily. Although this overall trend is observed for all droplet sizes, the dependence for smaller droplets tends more towards a linear relationship, while for bigger droplets, the dependence seems to exhibit non-linear characteristics.
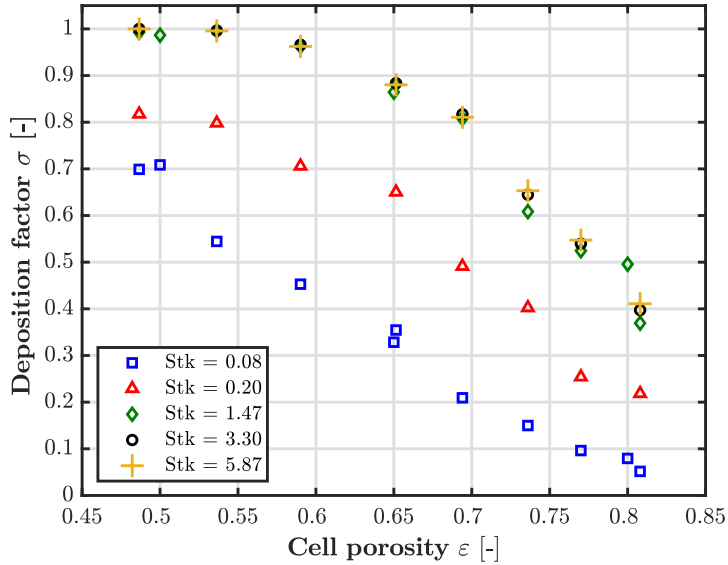

Figure 8: The dependence of cell porosity on the deposition factor σ for various droplets with diameters of $d_d = 5$, 8.2, 22, 33 and 40 µm with a constant inlet velocity of $0.6\,\mathrm{m\,s^{-1}}$, corresponding to the Stokes number in legend.

An increase in cell porosity may influence the cell permeability in two ways. First, as mentioned above, an increase in porosity increases the probability of a droplet having its path blocked by a particle, effectively shortening its mean free path. This effect is independent of the droplet size. Second, an increase in porosity makes the path of the droplet more tortuous. The relation between porosity and tortuosity is widely studied in literature [26, 41, 49]: the consensus is that tortuosity has a more or less linear (or sometimes super linear) dependence on the porosity. Because of that, droplets need to follow a more curved trajectory which results in a higher deposition factor.

21

This effect has a different impact on fine and large droplets. Larger droplets, characterized by a higher Stokes number, have more inertia and are therefore less likely to adhere to the curved gas trajectory, resulting in a higher deposition rate. Smaller droplets respond more directly to changes in the gas flow direction and can more easily maneuver around obstacles, resulting in a lower deposition rate. For this reason, the deposition rate shows a linear behavior toward cell porosity for smaller droplets (the effect of increased tortuosity is small) and a non-linear behavior for bigger droplets, especially for low values of porosity (both the effects of an increase in tortuosity and shorter mean free path are significant).

4.2. Influence of particle Reynolds number

Increasing the particle Reynolds number will usually result in a more chaotic motion of the fluid around the particle. In regard to droplets dispersed in the fluid, it is expected that this change in flow pattern also affects the deposition of droplets. As the chaotic motion intensifies as a function of the particle Reynolds number, fluid streamlines will become more disordered. As a result, droplets can more easily detach from said streamlines, leading to a higher deposition factor. The actual dependence on the particle Reynolds was investigated by performing two series of simulations for two droplets with fixed Stokes numbers $Stk = 0.22$ and 0.38. The porosity of the domain was held constant at a value of $\varepsilon = 0.65$ and the Reynolds number was varied systematically between 100 – 350. For the cases of $Re_p = 100$ and $Re_p = 130$ this was accomplished by changing the particle diameter from to $5 \cdot 10^{-4}$ m to $3 \cdot 10^{-4}$ m and $2.5 \cdot 10^{-4}$ m respectively, while keeping the inlet velocity constant at $0.6\,\mathrm{m\,s^{-1}}$. For the case of $Re_p = 210$, $Re_p = 270$ and $Re_p = 320$, the particle diameter was held constant at $5 \cdot 10^{-4}$ m and the inlet gas velocity was changed systematically from 0.6 to 0.95 $\mathrm{m\,s^{-1}}$. The droplet diameter was changed accordingly to maintain a constant Stokes number. Each simulation was repeated three times, and the results are presented in Figure 9.
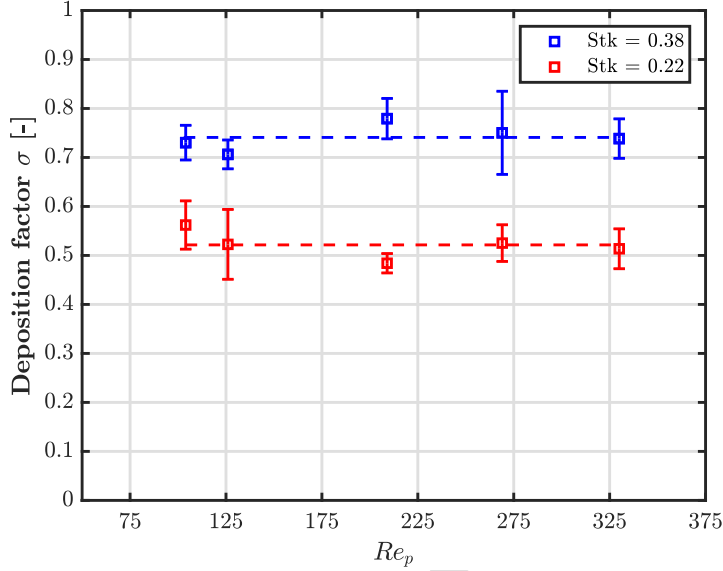
Figure 9: Deposition factor dependence of particle Reynolds number for Stokes numbers of 0.22 and 0.38 and a porosity of $\varepsilon = 0.65$

For both Stokes numbers, no effect of the particle Reynolds number was observed, which is in disagreement with initial expectations and results reported by Kirsh and Kirsh [23], where droplet deposition in the context of granular filtration depends on the particle Reynolds number.

However, it should be noted that in the latter study the dependence on Re was only investigated for values $Re_p < 50$, which is significantly lower than encountered in a typical fluidized bed. Coury et al. [4] and Kolakaluri [25] investigated cases with higher Reynolds numbers. In their work, they concluded that a dependence on the particle Reynolds number is only observed at low Reynolds numbers ($Re_p < 10$). For higher values of Re_p only a weak or no dependence of Re_p was found (respectively at $10 < Re_p < 100$ and $Re_p > 100$). These findings are in agreement with results presented in this work: no effect of the particle Reynolds number, provided that the Stokes number is held constant.

4.3. Influence of Stokes number

To investigate the dependence of droplet Stokes number, the droplet diameter, and the gas velocity were varied independently. A first set of simulations was performed with the droplet diameter varied from 5 to 40 µm, porosity ranging between 0.4 and 0.8, while the gas inlet velocity was kept constant at a value of $0.6\,\mathrm{m\,s^{-1}}$. A second set of simulations was performed with the same interval of droplet diameters, but with a fixed porosity of $\varepsilon = 0.7$ and a gas inlet velocity ranging between 0.15 and $1.5\,\mathrm{m\,s^{-1}}$. The two sets result in an investigated interval of Stokes number $0.34 < Stk < 218$.
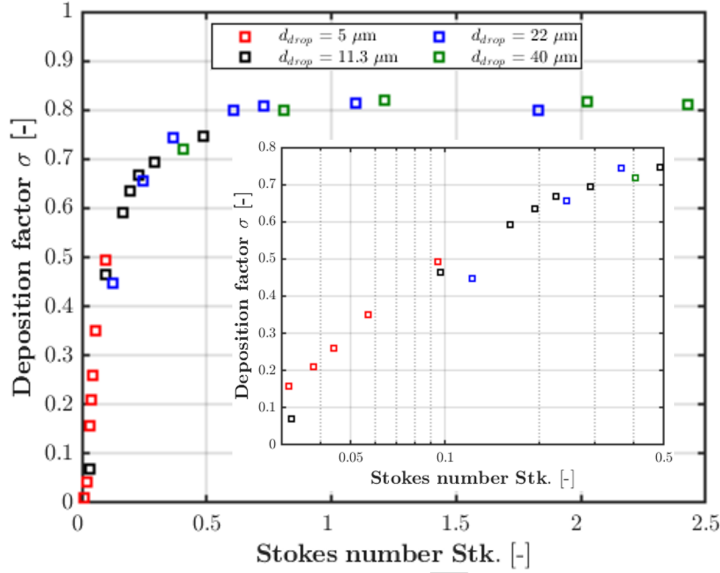
Figure 10: Dependence of the deposition factor on the droplet Stokes number at a porosity $\varepsilon = 0.7$

In Figure 10 it can be discerned that the deposition factor increases with increasing droplet Stokes number, in accordance with physical and bibliographical expectation: a greater Stokes number means droplets have more inertia and a longer relaxation time, therefore they tend to follow their own trajectory rather than the gas flow, resulting in an increased deposition rate on the particle surface. It is interesting to notice that the deposition factor shows an asymptotic behavior: in the case of $\varepsilon = 0.7$, σ becomes constant for $Stk > 0.7$ at a value of $\sigma \simeq 0.8$. An explanation might be that at high Stokes numbers droplets have enough inertia to not be significantly influenced by the fluid and instead only continue along their initial trajectory. Further increasing the droplet Stokes number would then only lead to an increase in inertia and so would not result in more deposition, as the droplets already follow their own path.

In addition, simulations performed at larger values of porosity show a lower asymptotic value of the deposition factor (see Fig. 13), suggesting that in cases where the porosity is larger preferred "open" pathways for the gas prevail, through which part of the droplets are able to escape the bed without encountering a particle.

4.4. Extension to longer domains

As a droplet traverses through the static array of particles, the probability of it depositing on the particle surface increases, resulting in a dependence of the deposition factor on the domain length.

Since the main objective of this work is to formulate closures to be implemented in a coarse grained model (CFD-DEM), it is of paramount importance to assess the possibility to calculate the deposition factor of longer domains as the combination of the deposition

24

factors of several smaller domains. In order to carry this investigation the approach depicted in Figure 12 was followed.
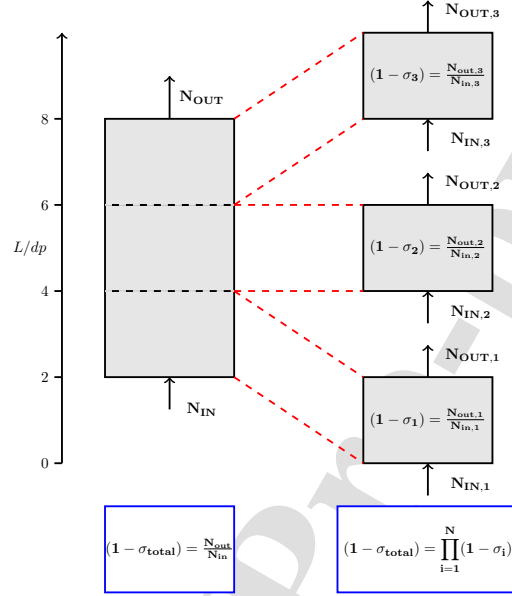

Figure 11: Visual depiction of the approach used to model the deposition of droplets in larger domains using the results from smaller subdomains

The relation between the overall deposition factor (σ_{total}) and the deposition factor of N individual subdomains (σ_i) is given by Equation 15

$$1 - \sigma_{total} = \prod_{i=1}^{N} (1 - \sigma_i) \tag{15}$$

When the large domain consists of smaller subdomains that are of equal length, porosity and Stokes number, then Equation 15 reduces to a simpler form presented in Equation 16

$$1 - \sigma_{total} = (1 - \sigma_1)^{L_{tot}/L_{sub}} \tag{16}$$

The theoretically derived deposition factor(s) were compared to real 'larger' scale simulations. This was done using domains with equal porosity so that predicted values can be calculated according to Equation 16. A comparison between the deposition factor obtained from the simulations (solid lines) and the predicted values (dashed lines) is presented in Figure 12.
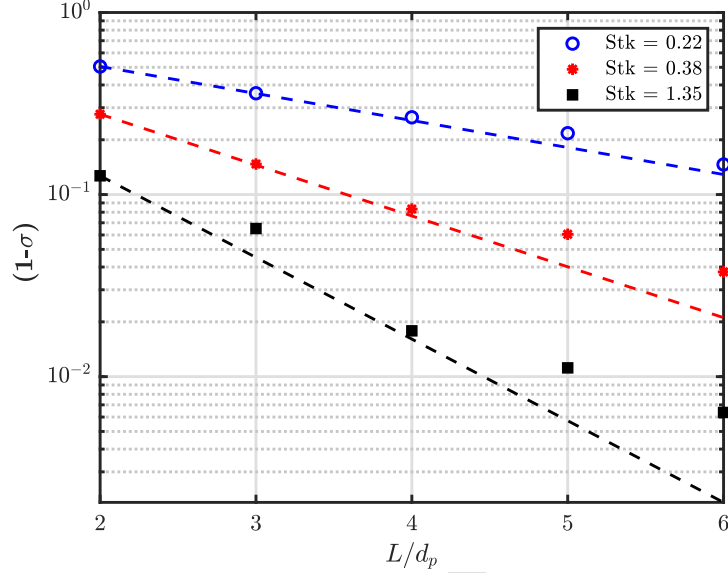
25

Figure 12: The dependence of the deposition factor as a function of the domain length, compared to the theoretically predicted values by Equation 16 (dashed lines), for Stokes numbers Stk = 0.22, 0.38 and 1.35 and a porosity of $\varepsilon = 0.65$.

As shown in Figure 12, the results from the simulations match the predicted values for all the intervals of length and Stk numbers investigated, with a maximum absolute error < 5% for the case with Stk=1.35. It can be concluded that the results from smaller domains can readily be extended to larger domains with the help of equations Equation 15 and Equation 16, without sacrificing too much accuracy.

4.5. Nonlinear regression

With the obtained data presented in the previous sections, a correlation was developed that can be used to describe the deposition of droplets in more coarse-grained models such as a Discrete Particle Model. The functional form of the correlation was not arbitrarily selected, but instead considering certain constraints, imposed to prevent the correlation from generating nonphysical results. The following constraints were imposed:

1. At Stk $\rightarrow$ 0 droplets should perfectly follow the fluid flow, without any deposition on the particle surface ($\sigma = 0$)
2. If the domain is empty ($\varepsilon = 1$ or $\phi = 0$), the domain contains no particles for droplets to deposit on, and so $\sigma = 0$.
3. σ should always be bounded between 0 and 1.

In addition to these constraints, the correlation should also be able to represent the overall behavior of the results. This means that as the Stokes number becomes greater than one, the deposition factor should tend to a constant value. In addition, as the

26

cell porosity goes to its maximum value, the deposition factor should approach unity. Based on these considerations and constraints, the candidate function as presented in Equation 17 was formulated.

$$\sigma^{-1} = (1 + e^{-(k_1\,\phi^{-1}+k_2\,\phi^2+k_3\,S_{tk}^{-1})})(1 + e^{-(k_4+k_5\,Stk)}) \tag{17}$$

Equation 17 satisfies all the requirements: $\sigma = 0$ for $\phi = 0$ due the term $k_1\,\phi^{-1}$ ($k_1 < 0$), $\sigma = 0$ for $Stk = 0$ due the term $k_3\,Stk^{-1}$ and the overall shape of the function matches the data obtained by the model.

The estimation of fitting parameters $k_{1,\dots 5}$ was performed with a nonlinear regression of the data presented in the previous section on Equation 17. The software of choice is MATLAB, using the built-in function *nlinfit*, which uses a nonlinear least-squares algorithm to estimate the correlation coefficients. The values found from this procedure are presented in Table 7. The significance of the parameters was assessed by computing their 95 % confidence interval using MATLAB's built-in function *nlparci*. These confidence intervals are reported alongside the fitted parameter in Table 7: as none of the intervals contain a zero it can be concluded that all parameter have a significant contribution and so are required in the model.

Table 7: List of the optimal fitted parameters and their confidence interval obtained using nonlinear regression

Parameter	Value	95% CI		
k_1	-0.1876	[-0.2063	;	-0.1690]
k_2	20.6178	[21.66	;	19.5698]
k_3	-0.1726	[-0.1834	;	-0.1617]
k_4	0.7117	[0.5141	;	0.9092]
k_5	4.1107	[3.124	;	5.097]

In figures Figure 14 and Figure 13 a comparison between the model data and the fit is presented.
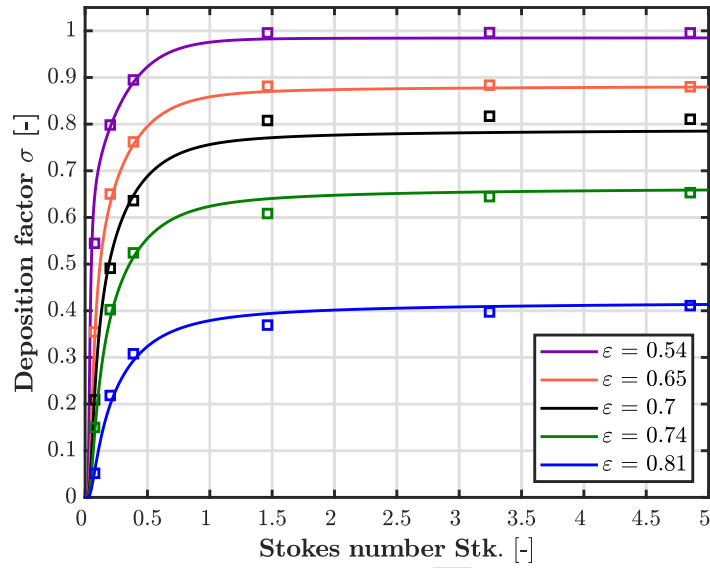
27

Figure 13: Comparison between the deposition factor calculated from simulations and predicted by Equation 17 with parameters in Table 7 as function of the Stokes number.
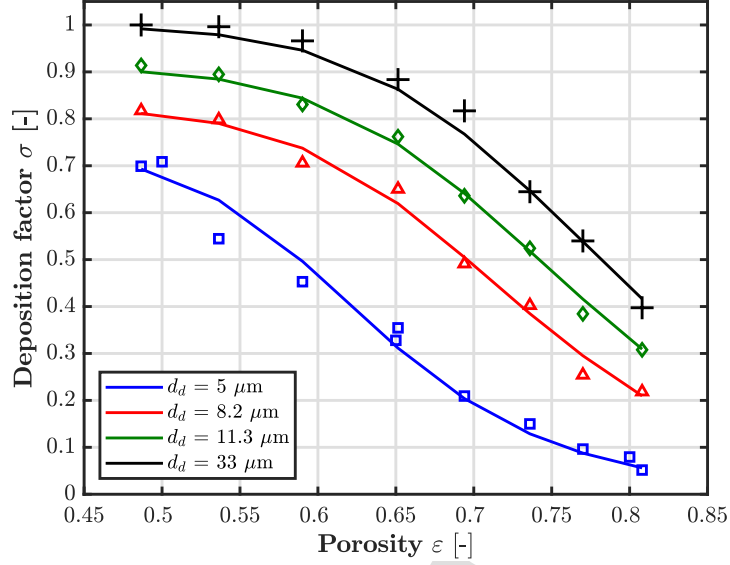
28

Figure 14: Comparison between the deposition factor calculated from simulations and predicted by Equation 17 with parameters in Table 7 as function of the porosity ε.

The developed correlation is capable of accurately describing the dependency of deposition factor with the Stokes number for all the investigated porosity intervals. However, the correlation loses some accuracy in predicting the dependency of the deposition factor on the porosity for low droplet sizes ($d_d = 5\mu m$) in a porosity interval between 0.5 and 0.65. For all the other droplet sizes, the correlation retains its accuracy.

To further assess the validity and accuracy of the developed correlation, the deposition factor from all simulations were compared to the deposition factor predicted by the correlation (Equation 17) in a parity plot shown in Figure 15. Here it can be noticed that, except for very few points, all the data falls inside the 15 % error band. The points not following this trend all located at lower deposition factors and present a tolerable absolute deviation from the correlation. This is highlighted in Figure 16, where the difference between the predicted and calculated deposition factor is reported for every simulation. It can be noted that not only are the errors always smaller than ±0.1, but the deviations are also scattered around zero, showing that there is no systematic under- or over-prediction by the correlation.

While the functional dependency of the developed correlation (Eq. 17) is valid for all domain sizes, the calculated values of the fitting parameters $k_{1,\ldots 5}$ are specific for the analyzed domain length L. In order to extend its applicability to a domain of arbitrary size L_a, an overall deposition factor σ_{total} can be calculated from Eq. 16 and from it a droplet mass deposition rate S (in $kg/m^2 s$) can be calculated as:
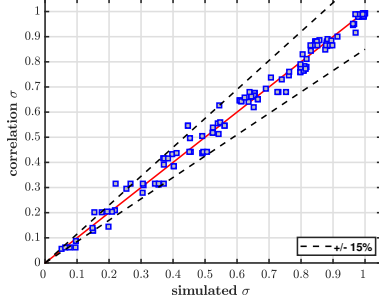
29

Figure 15: Parity plot of the deposition factor from simulation data of the vs. the deposition factor predicted by Equation 17. The dashed lines represent ±15% error bounds
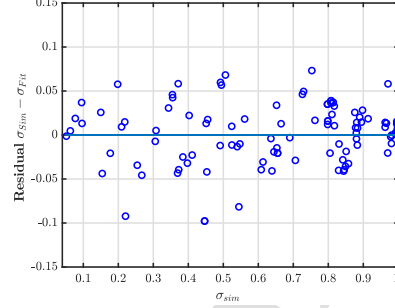
Figure 16: Residual plot of the deposition factor from all simulation data of the vs. the deposition factor predicted by Equation 17.

$$S = \rho_d \varepsilon_d u_z \sigma_{total} \tag{18}$$

where u_z is the local gas velocity in the stream-wise direction (vertical flow is assumed for simplicity) and ε_d is the local droplet phase fraction.

5. Comparison with experimental data

As mentioned, most of the experimental data available in the open literature are obtained using droplet diameters much smaller than the one under investigation in this work, and can therefore not be used for model validation. An exception is a data-set presented in [24], where an aerosol composed of droplets of $d_d = 2.9 \ \mu m$ is injected into a fluidized bed composed of particles of size $4.25 \cdot 10^{-4} m$ with a gas velocity of $0.168 \ m/s$, and the deposition factor was reported for different bed heights. While the droplet size is, strictly speaking, outside the range under analysis in the present work, the dataset is considered usable because: 1) The droplet size is big enough, so that the model's main assumption (i.e. inertial deposition is the main removal mechanism and Brownian diffusion is negligible) holds; 2) The droplet Stokes number was $Stk \approx 0.025$, i.e. within the investigated range.

No measurement of the average bed porosity was reported, and it has been estimated to be approximately $\varepsilon = 0.45$ and was considered constant in the whole bed. Results are presented in Figure 17, where model results are obtained by combining Eqs. 16 and 17.
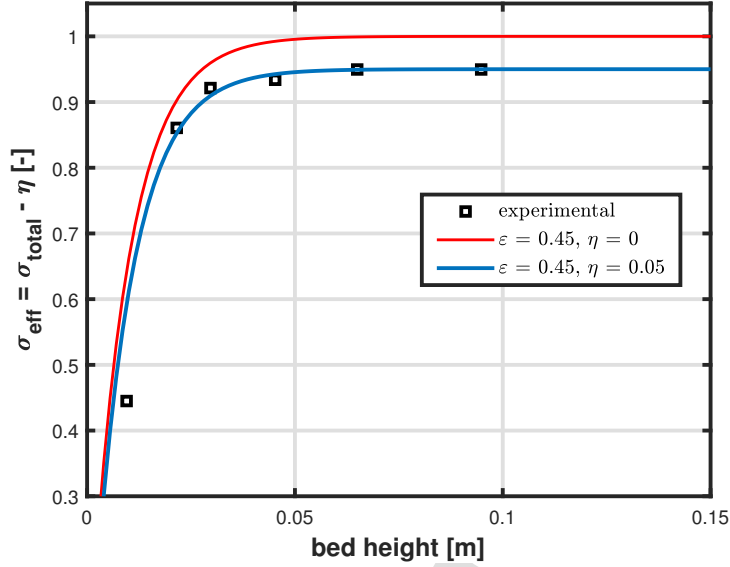
30

Figure 17: Comparison of deposition factor as measured in [24] (experimental) and predicted by this work.

It can be noticed that the model *"as it is"* overestimates the droplets deposition with about 5% at higher bed heights. This can be ascribed to:

- Entrainment of droplets from the particle surface to the gas phase (not accounted for in the presented model)

- Bypass of emulsion phase due the formation of bubbles (this effect cannot be captured when assuming constant bed porosity, but can be calculated in the larger scale CFD-DEM model)

The introduction of an inefficiency $\eta = 0.05$ leads to a very good description of experimental data as a function of the bed height.

6. Conclusion

In this study, the permeability of droplets in a fluidized bed was investigated to develop a correlation for the rate of deposition of liquid droplets on the particle surface using a novel liquid injection model, developed within the open-source CFD framework OpenFOAM v7. All the steps constituting the liquid injection model were extensively tested to assess its robustness. First, the implementation of the Eulerian solver was verified through several test cases involving a grid dependency study, verification through analytical solutions and with empirical drag correlations. From these simulations, it was concluded that the implementation was performed successfully, yielding a reliable and accurate flow field.

31

An analysis of the transient gas flow was then performed, highlighting its pseudo-periodical structure. The effect of such conditions on droplet deposition was investigated by both injecting droplets at different times and using a time-averaged flow field: it was concluded that the effect on the deposition factor is negligible. In addition, the statistical robustness of the model was assessed performing a Monte Carlo convergence test, where the number of injected droplets was varied.

To investigate the influence of the simulation geometry (i.e. the particle configuration) a study was performed, testing various particle configurations resulting from a CFD-DEM simulation or generated with the Lubachevsky-Stillinger algorithm with periodic boundary conditions for the gas phase. It was found that the deposition factor does not significantly depend on the specific particle configuration, provided that lateral escaping and entering droplets are accounted for. It is therefore unnecessary to generate a particle configuration using a complex model such as a CFD-DEM and instead it can be artificially generated by a suitable packing algorithm, allowing the model to be faster and easier to reproduce.

The characterization of fluidized bed permeability was performed investigating the effects of three dimensionless variables on the deposition factor: droplets Stokes number (Stk), particles Reynolds number (Re_p), and the domain porosity (ε). As a result, a strong dependence of the deposition factor on both porosity ε and on Stk was found, whereas the dependence on the particles Reynolds number was negligible for a constant Stokes number. These findings are in accordance with physical expectations and coherent with what is reported in literature.

In addition, the possibility to combine the deposition factor of multiple small-scale simulations to emulate larger scale simulations was demonstrated. This confirmed the extendibility of the model to a larger scale without having to perform computationally expensive large-scale simulations.

From the results presented in this work, a correlation was derived that can be used to describe the deposition of droplets in more coarse-grained models such as a discrete particle model for different conditions of Stk and porosity. The functional form of the correlation was selected considering several physical constraints, imposed to prevent the correlation from generating nonphysical results. In this work, it was found that not only the optimal fitted parameters can be determined with reasonable certainty, but it was also shown that the developed correlation can fit the previous simulation data accurately while also being capable of predicting values for future simulations. A statistical analysis performed on the regression assured physical significance for all the fitting parameters, all showing reasonably narrow confidence intervals.

Future work should also investigate the effects that rotation and translation of the particles may have of the gas flow and, eventually, on the droplet deposition factor: while in this work the average droplet velocity was assumed to be much higher than the particle velocity, there may still be an effect induced by the increase in particle-gas relative velocity and particle displacement.

References

[1] S Balachandar and John K Eaton. Turbulent dispersed multiphase flow. *Annual review of fluid mechanics*, 42:111–133, 2010.

[2] R Beetstra, Martin Anton van der Hoef, and JAM Kuipers. Drag force of intermediate reynolds number flow past mono-and bidisperse arrays of spheres. *AIChE journal*, 53(2):489–501, 2007.

[3] Shanshan Bu, Jian Yang, Qingtai Dong, and Qiuwang Wang. Experimental study of transition flow in packed beds of spheres with different particle sizes based on electrochemical microelectrodes measurement. *Applied thermal engineering*, 73(2):1525–1532, 2014.

[4] JR Coury, KV Thambimuthu, and R Clift. Capture and rebound of dust in granular bed gas filters. *Powder technology*, 50(3):253–265, 1987.

[5] JF De Jong, TYN Dang, M van Sint Annaland, and JAM Kuipers. Comparison of a discrete particle model and a two-fluid model to experiments of a fluidized bed with flat membranes. *Powder technology*, 230:93–105, 2012.

[6] NG Deen, M Van Sint Annaland, Martin Anton Van der Hoef, and JAM Kuipers. Review of discrete particle modeling of fluidized beds. *Chemical engineering science*, 62(1-2):28–44, 2007.

[7] A Della Torre, G Montenegro, A Onorati, and G Tabor. Cfd characterization of pressure drop and heat transfer inside porous substrates. *Energy Procedia*, 81:836–845, 2015.

[8] MM El-Halwagi. Mathematical modeling of aerosol collection in fluidized-bed filters. *Aerosol science and technology*, 13(1):102–115, 1990.

[9] Said Elghobashi. On predicting particle-laden turbulent flows. *Applied scientific research*, 52(4): 309–329, 1994.

[10] Sabri Ergun. Fluid flow through packed columns. *Chem. Eng. Prog.*, 48:89–94, 1952.

[11] Joel H Ferziger, Milovan Perić, and Robert L Street. *Computational methods for fluid dynamics*, volume 3. Springer, 2002.

[12] The OpenFOAM Foundation. *OpenFOAM v7 User Guide*, 2020. URL https://cfd.direct/openfoam/user-guide.

[13] The OpenFOAM Foundation. Mesh generation with the snappyhexmesh utility, 2020. URL https://cfd.direct/openfoam/user-guide/v8-snappyHexMesh/.

[14] MJV Goldschmidt, GGC Weijers, R Boerefijn, and JAM Kuipers. Discrete element modelling of fluidised bed spray granulation. *Powder technology*, 138(1):39–45, 2003.

[15] Don W Green. *Perry's chemical engineers'*. McGraw Hill, 1986.

[16] T Horneber, C Rauh, and A Delgado. Fluid dynamic characterisation of porous solids in catalytic fixed-bed reactors. *Microporous and mesoporous materials*, 154:170–174, 2012.

[17] Michael Hounslow. The population balance as a tool for understanding particle rate processes. *KONA Powder and Particle Journal*, 16:179–193, 1998.

[18] Simon M Iveson. Limitations of one-dimensional population balance models of wet granulation processes. *Powder Technology*, 124(3):219–229, 2002.

[19] Simon M Iveson, James D Litster, Karen Hapgood, and Bryan J Ennis. Nucleation, growth and breakage phenomena in agitated wet granulation processes: a review. *Powder technology*, 117(1-2): 3–39, 2001.

[20] Zhaochen Jiang, Andreas Bück, and Evangelos Tsotsas. Cfd-dem study of residence time, droplet deposition, and collision velocity for a binary particle mixture in a wurster fluidized bed coater. *Drying Technology*, 36(6):638–650, 2018.

[21] Zhaochen Jiang, Christian Rieck, Andreas Bück, and Evangelos Tsotsas. Modeling of inter-and intra-particle coating uniformity in a wurster fluidized bed by a coupled cfd-dem-monte carlo approach. *Chemical Engineering Science*, 211:115289, 2020.

[22] DK Kafui and C Thornton. Fully-3d dem simulation of fluidised bed spray granulation using an exploratory surface energy-based spray zone concept. *Powder Technology*, 184(2):177–188, 2008.

[23] VA Kirsh and AA Kirsh. Nanoparticle deposition in granular filters at reynolds numbers higher than unity. *Colloid Journal*, 79(4):481–486, 2017.

[24] Pavel Knettig and JM Beeckmans. Capture of monodispersed aerosol particles in a fixed and in a fluidised bed. *The Canadian Journal of Chemical Engineering*, 52(6):703–706, 1974.

[25] Ravi Kolakaluri. "direct numerical simulations and analytical modeling of granular filtration", 2013.

[26] Antti Koponen, M Kataja, and J v Timonen. Tortuous flow in porous media. *Physical Review E*, 54(1):406, 1996.

[27] D Kumar, T Sikroria, A Kushari, et al. A twin-fluid injector for fcc feed injection. *Int J Petrochem Sci Eng*, 4(3):109–115, 2019.

[28] Z Li, M van Sint Annaland, JAM Kuipers, and NG Deen. Effect of superficial gas velocity on the

33

particle temperature distribution in a fluidized bed with heat production. *Chemical Engineering Science*, 140:279–290, 2016.

[29] Francesco Lucci, Augusto Della Torre, Jan von Rickenbach, Gianluca Montenegro, Dimos Poulikakos, and Panayotis Dimopoulos Eggenschwiler. Performance of randomized kelvin cell structures as catalytic substrates: mass-transfer based analysis. *Chemical Engineering Science*, 112: 143–151, 2014.

[30] Wang-Yu Ma and Zheng-Hong Luo. Operating stability analysis of continuous gas–liquid–solid fbr under super-condensed mode. *Advanced Powder Technology*, 30(4):751–765, 2019.

[31] Daniel McCarthy, Anthony J Yankel, Ronald G Patterson, and Melbourne L Jackson. Miltistage fluidized bed collection of aerosols. *Industrial & Engineering Chemistry Process Design and Development*, 15(2):266–272, 1976.

[32] Timothy FL McKenna. Condensed mode cooling of ethylene polymerization in fluidized bed reactors. *Macromolecular Reaction Engineering*, 13(2):1800026, 2019.

[33] Banks Michael and E Aulton Michael. Fluidised-bed granulation: a chronology. *Drug development and industrial pharmacy*, 17(11):1437–1463, 1991.

[34] Milan Mihajlovic, Ivo Roghair, and Martin Van Sint Annaland. On the numerical implementation of the van der waals force in soft-sphere discrete element models for gas-solid fluidization. *Chemical Engineering Science*, page 115794, 2020.

[35] Parviz Moin and Krishnan Mahesh. Direct numerical simulation: a tool in turbulence research. *Annual review of fluid mechanics*, 30(1):539–578, 1998.

[36] AW Nienow. Fluidised bed granulation and coating: applications to materials, agriculture and biotechnology. *Chemical Engineering Communications*, 139(1):233–253, 1995.

[37] Vishal A Patil and James A Liburdy. Scale estimation for turbulent flows in porous media. *Chemical Engineering Science*, 123:231–235, 2015.

[38] Alkiviades C Payatakes, Chi Tien, and Raffi M Turian. A new model for granular porous media: Part i. model formulation. *AIChE Journal*, 19(1):58–67, 1973.

[39] MH Peters, Liang-Shih Fan, and TL Sweeney. Simulation of particulate removal in gas-solid fluidized beds. *AIChE Journal*, 28(1):39–49, 1982.

[40] Stephen B Pope. Turbulent flows, 2001.

[41] M Punčochář and J Drahoš. The tortuosity concept in fixed and fluidized bed. *Chemical engineering science*, 48(11):2173–2175, 1993.

[42] Reza Sadeghbeigi. *Fluid catalytic cracking handbook: An expert guide to the practical operation, design, and optimization of FCC units*. Butterworth-Heinemann, 2020.

[43] AS Sangani and A Acrivos. Slow flow through a periodic array of spheres. *International Journal of Multiphase Flow*, 8(4):343–360, 1982.

[44] L. Schiller and Z. Naumann. "a drag coefficient correlation,". *VDI Zeitung*, Vol. 77:318–320, 1935.

[45] DS Scott and DA Guthrie. Removal of a mist in a fluidized bed. *The Canadian Journal of Chemical Engineering*, 37(5):200–203, 1959.

[46] Qiang Shi, Shaoshuo Li, Sihang Tian, Zhengliang Huang, Yao Yang, Zuwei Liao, Jingyuan Sun, Jingdai Wang, and Yongrong Yang. Investigating agglomeration behaviors in high temperature gas–solid fluidized beds with liquid injection. *Industrial & Engineering Chemistry Research*, 57 (15):5482–5494, 2018.

[47] Monica Skoge, Aleksandar Donev, Frank H Stillinger, and Salvatore Torquato. Packing hyperspheres in high-dimensional euclidean spaces. *Physical Review E*, 74(4):041127, 2006.

[48] PG Smith and AW Nienow. Particle growth mechanisms in fluidised bed granulation—i: the effect of process variables. *Chemical Engineering Science*, 38(8):1223–1231, 1983.

[49] Zufeng Sun, Xiaowu Tang, and Guanchu Cheng. Numerical simulation for tortuosity of porous media. *Microporous and Mesoporous Materials*, 173:37–42, 2013.

[50] Vinayak S Sutkar, Niels G Deen, Amit V Patil, Vitalij Salikov, Sergiy Antonyuk, Stefan Heinrich, and JAM Kuipers. Cfd–dem model for coupled heat and mass transfer in a spout fluidized bed with liquid injection. *Chemical Engineering Journal*, 288:185–197, 2016.

[51] Lianghui Tan, Ivo Roghair, and Martin van Sint Annaland. Discrete particle simulations of bubble-to-emulsion phase mass transfer in single-bubble fluidized beds. *Particuology*, 33:80–90, 2017.

[52] Y Tang, EAJF (Frank) Peters, JAM (Hans) Kuipers, SHL (Sebastian) Kriebitzsch, and MA (Martin) van der Hoef. A new drag correlation from fully resolved simulations of flow past monodisperse static arrays of spheres. *AIChE journal*, 61(2):688–698, 2015.

[53] G Tardos, Nesim Abuaf, and Chaim Gutfinger. Diffusional filtration of dust in a fluidized bed. *Atmospheric Environment (1967)*, 10(5):389–394, 1976.

[54] K Ushiki and Chi Tien. Calculation of aerosol collection in fluidized filter beds. *AIChE journal*, 30

(1):156–168, 1984.

[55] AA Zick and GM Homsy. Stokes flow through periodic arrays of spheres. *Journal of fluid mechanics*, 115:13–26, 1982.

[56] I Ziółkowska and D Ziółkowski. Fluid flow inside packed beds. *Chemical Engineering and Processing: Process Intensification*, 23(3):137–164, 1988.

- CFD-DEM simulation of liquid droplets permeating a particle array was performed
- Gas flow between the particles was simulated on Eulerian mesh
- Droplet deposition factor on the particles was analysed and a correlation was proposed
- Deposition factor dependence on the Stokes number and porosity has been quantified
- Deposition probability can be scaled to particle arrays of arbitrary length

- DM Balice: Conceptualization; Methodology; Writing - Original Draft; Writing - Review & Editing; Formal analysis; Supervision

- CWC Molenaar: Methodology; Writing - Original Draft; Software; Validation; Formal analysis; Investigation; Visualization

- M Fochesato: Methodology; Software; Investigation

- CM Venier: Software

- I Roghair: Conceptualization; Supervision; Funding acquisition; Project administration; Supervision

- NG Deen: Conceptualization; Supervision; Funding acquisition; Project administration; Supervision

- M van Sint Annaland: Conceptualization; Supervision; Funding acquisition; Project administration; Supervision

Declaration of interests

☐ The authors declare that they have no known competing financial interests or personal relationships that could have appeared to influence the work reported in this paper.

☒ The authors declare the following financial interests/personal relationships which may be considered as potential competing interests: